Research Article

Journal of Environmental Nanotechnology

Development and Characterization of $MnFe_2O_4$-Nanocellulose Hybrid Nanocomposites for Advanced Functional Applications

Sandeep Gupta[1], A. Rajkumar[2*], Prabahar jeevanandam[3], S. Arunkumar[4], N. Bala Krishnan[5] and Jarupula Somlal[6]

[1]Department of Electrical Engineering, Graphic Era (Deemed to be University), Dehradun, UK, India
[2]Department of Mechanical Engineering, Rajalakshmi Engineering College, Kancheepuram, TN, India
[3]Department of Mechanical engineering, Park College of Engineering and Technology, Coimbatore, TN, India
[4]Department of Mechanical Engineering, Vinayaka Mission's Kirupananda Variyar Engineering College, Vinayaka Mission's Research Foundation (Deemed to be University), Salem, TN, India
[5]Department of Manufacturing Engineering, Vinayaka Mission's Kirupananda Variyar Engineering College, Vinayaka Mission's Research Foundation (Deemed to be University),Salem, TN, India
[6]Department of Electrical and Electronics Engineering, Koneru Lakshmaiah Education Foundation, Vaddeswaram, Guntur, AP, India
Received: 28.03.2026 Accepted: 25.05.2026 Published: 30.06.2026
*rajkumaraccmail01@gmail.com

ABSTRACT

Development of multifunctional nanocomposite materials based on natural fibers and magnetic oxides remains challenging due to nanoparticle agglomeration and weak interaction between inorganic nanoparticles and biodegradable fiber matrices. In this work, a hybrid nanocomposite was developed using manganese ferrite ($MnFe_2O_4$) nanoparticles and nanocellulose fibers derived from bamboo as a sustainable reinforcing matrix. $MnFe_2O_4$ nanoparticles were synthesized by sol–gel auto-combustion method employing iron nitrate and manganese nitrate precursors with glycine as a fuel–chelating agent, while nanocellulose fibers were obtained from bamboo cellulose through alkali treatment, bleaching, and TEMPO-mediated oxidation. The $MnFe_2O_4$–nanocellulose composites were prepared in two weight ratios (50:50 and 75:25) through dispersion, ultrasonication, filtration, and drying processes. Structural and morphological characterization was carried out using XRD, FTIR, SEM, and EDAX analyses. The XRD results confirmed the formation of spinel $MnFe_2O_4$ with crystallite sizes in the range 15–20 nm, while nanocellulose fibers exhibited crystallite sizes of approximately 20–30 nm. The SEM analysis revealed that $MnFe_2O_4$ nanoparticles had particle sizes ranging from 60–120 nm, whereas nanocellulose fibers showed diameters between 15 and 35 nm. The composite samples displayed particle size distributions of 60–120 nm for the 50:50 composition and 40–110 nm for the 75:25 composition, indicating effective dispersion of ferrite nanoparticles within the nanocellulose matrix. The EDAX analysis further confirmed the presence of Mn, Fe, O, and C elements, validating the successful formation of hybrid composite structure. The synthesized $MnFe_2O_4$–nanocellulose nanocomposites exhibit porous morphology, high surface area, and improved structural stability, making them promising materials for gas sensing, environmental monitoring, catalytic systems, and advanced functional nanomaterial applications.

Keywords: Natural fibers; Ultrasonication; XRD; Manganese ferrite nanoparticles; SEM.

1. INTRODUCTION

Hybrid nanostructured materials combining magnetic oxides with natural nanofibers have attracted increasing interest due to their enhanced physicochemical, magnetic, and multifunctional properties suitable for advanced electrical and environmental applications. Among them, manganese ferrite ($MnFe_2O_4$) integrated with cellulose nanofibers offers improved structural stability, reduced nanoparticle agglomeration, and enhanced functional performance through the formation of interconnected hybrid nanocomposite networks. Several synthesis strategies such as green synthesis, co-precipitation, and sol–gel methods have been reported for producing $MnFe_2O_4$ nanoparticles with controlled morphology and functional properties. Green synthesis using plant extracts has recently gained importance because it provides an environmentally friendly approach for nanoparticle fabrication. For instance, $MnFe_2O_4$ nanoparticles synthesized using Salvadora persica extract and incorporated into $MnFe_2O_4$/CMC nanocomposites demonstrated enhanced catalytic degradation of amoxicillin, achieving up to 97% degradation efficiency (Riaz *et al.* 2024).

Various compositional modifications and doped ferrite systems have also been explored to enhance structural and functional properties of manganese ferrites. Nickel-substituted ferrite nanoparticles ($Ni_xMn_{1-x}Fe_2O_4$) synthesized through the co-precipitation technique exhibited cubic spinel structure and spherical morphology, indicating improved structural stability (Oviya and Sivagurunathan, 2024). Similarly,

polyethylene glycol (PEG)-functionalized $MnFe_2O_4$ nanoparticles synthesized by the co-precipitation method displayed enhanced magnetic and dielectric properties due to improved particle dispersion (Ullah *et al.* 2026). Rare-earth doping and metal substitution have also been widely used to modify ferrite structures. Yb^{3+}-doped $Zn_{0.9}Mg_{0.1}Fe_{2-x}Yb_xO_4$ nano-ferrites prepared by the sol–gel auto-combustion method exhibited crystallite sizes in the range 33–41 nm and demonstrated strong photocatalytic degradation of RhB dye under sunlight irradiation (Dhasharatha *et al.* 2024). Similarly, aluminum-doped $Zn_{0.5}Mn_{0.5}Fe_2O_4$ photocatalysts synthesized through the sol–gel method showed reduced bandgap energy and achieved 95% atrazine degradation under visible light conditions (Yasar and Javed, 2025).

Hybrid nanocomposites combining ferrites with carbon-based or polymeric materials have been widely investigated to enhance adsorption and catalytic performance. Reduced graphene oxide (rGO)-incorporated $MnFe_2O_4$ nanocomposites synthesized by reduction photolysis demonstrated excellent catalytic activity, achieving nearly 100% CO conversion at 80 °C with high stability (Mahmoud *et al.* 2024). Similarly, magnetically separable $MnFe_2O_4$@BAC nanohybrids prepared from activated carbon derived from black cumin waste exhibited a high oxytetracycline adsorption capacity of 591.7 mg g^{-1} with excellent reusability (Teymur and Güzel, 2024). In addition, Zn-modified manganese ferrite nanoparticles ($Mn_{0.8}Zn_{0.2}$ Fe_2O_4) synthesized by co-precipitation showed improved sorption capacity for rare-earth and heavy metal ions, following pseudo-second-order kinetics and Sips isotherm adsorption behavior (Ghaly *et al.* 2024). These research works highlight versatility of ferrite-based nanomaterials in catalytic and adsorption-based environmental applications.

Natural fibers have also been extensively investigated as sustainable reinforcement materials due to their low density, biodegradability. Bamboo fibers have attracted attention for use in composites and functional materials. Thermal aging studies on bamboo fibers demonstrated that exposure to temperatures between 60°C and 220°Csignificantly affects their physico-chemical properties, leading to structural degradation and crack formation as confirmed by FTIR, XRD, and SEM analyses (Fourari *et al.* 2026). Magnetic bamboo fibers prepared through lumen-loading methods using cobalt ferrite nanoparticles exhibited ferrimagnetic behavior and inverse spinel structures, indicating potential applications in magnetic recording and smart materials (Vermani *et al.* 2024). Furthermore, mechanochemical extraction and alkali treatment methods have been shown to enhance the crystallinity and thermal stability of bamboo fibers, making them suitable reinforcements for fiber-reinforced polymer composites (Verma *et al.* 2023; Asmare *et al.* 2024). Additional surface modification techniques such as vacuum-pressure impregnation and tannic acid treatment have further improved bamboo fiber performance in FRP composites (Verma *et al.* 2026).

Characterization method play critical role in understanding structural and morphological properties of nanomaterials and composites. Scanning Electron Microscopy (SEM) is widely used to investigate surface morphology, particle size distribution, and microstructural features at high resolution by scanning a focused electron beam across the material surface (Chakkour *et al.* 2024).

Recent studies have also explored advanced ferrite compositions for energy and electromagnetic applications. $MnFe_2O_4$/NiO nanocomposites synthesized by the sol–gel auto-combustion method have shown promising electrochemical performance for energy storage systems (Amjad *et al.* 2026). $MnFe_2O_4$ spinel nanoparticles synthesized by sol–gel techniques exhibited a bandgap of 2.64 eV, indicating potential optoelectronic applications (Hammou *et al.* 2025). Moreover, cobalt-doped $Mn_{1-x}Co_xFe_2O_4$ nanoparticles demonstrated improved dielectric properties and AC conductivity suitable for energy storage devices (Sarfraz *et al.* 2026), while cerium-substituted $MnFe_2O_4$ nanoparticles prepared using citrate-assisted sol–gel auto-combustion methods exhibited enhanced dielectric behavior and reduced magnetic saturation, making them suitable for electromagnetic shielding and high-frequency applications (Pandey *et al.* 2025).

A novel magnetic bio-nanocomposite integrating manganese ferrite nanoparticles with bamboo-derived nanocellulose fibers is developed to create a highly porous, high-surface-area hybrid material with enhanced gas-interaction capability, offering an eco-friendly and structurally stable alternative to conventional ferrite sensing materials while improving nanoparticle dispersion and functional response for advanced gas-sensing applications.

2. MATERIALS AND METHODS

Analytical-reagent grade iron(III) nitrate nonahydrate ($Fe(NO_3)_3 \cdot 9H_2O$) and manganese nitrate tetrahydrate ($Mn(NO_3)_2 \cdot 4H_2O$) were used as the metal precursors for the synthesis of manganese ferrite nanoparticles, while glycine acted as a fuel and chelating agent during the sol–gel auto-combustion process. All the chemicals of high purity were obtained from Matrics Enterprises, Nagercoil, Tamil Nadu, India. Nanocellulose fibers derived from bamboo were employed as the renewable reinforcing component and prepared through a controlled nanofibrillation process from natural bamboo fibers. Deionized distilled water served as the reaction medium and was utilized throughout all synthesis and experimental procedures to maintain uniformity and minimize contamination during the

preparation of the $MnFe_2O_4$–nanocellulose hybrid nanocomposite.

2.1 Synthesis of Manganese Ferrite Nanoparticles

Manganese ferrite nanoparticles were synthesized through sol–gel auto-combustion technique using metal nitrate precursors and glycine as a fuel–chelating agent. The molar proportion between the total metal nitrates and glycine was maintained at 1:3. Initially, $Fe(NO_3)_3 \cdot 9H_2O$ and $Mn(NO_3)_2 \cdot 4H_2O$ were dissolved separately in distilled water to prepare homogeneous precursor solutions. Approximately 20.19 g of $Fe(NO_3)_3 \cdot 9H_2O$ was dissolved in 25 mL of DI water to obtain 2 M ferric nitrate solution, while 7.27 g of $Mn(NO_3)_2 \cdot 4H_2O$ was dissolved in 25 mL of DI water to form 1 M manganese nitrate solution. The two precursor solutions were subsequently combined and stirred continuously using a magnetic stirrer to obtain a uniform mixed-metal solution. In a separate beaker, 11.26 g of glycine was dissolved in 50 mL of distilled water to prepare a 3 M fuel solution, which was then slowly introduced into the metal nitrate mixture under constant stirring. The resulting solution was heated to approximately 70 °C while stirring to promote complex formation between the metal ions and glycine. The pH of the solution was adjusted to around 7 by the gradual addition of ammonium hydroxide to stabilize the precursor sol.

After achieving the desired temperature and homogeneity, the solution was transferred into a preheated container with a large surface area placed on a heating mantle. Continued heating led to gradual evaporation of water and evolution of gases such as CO_2 and NO_x, causing the solution to thicken and transform into a viscous gel. Upon further heating, the gel underwent spontaneous auto-ignition, producing rapid combustion reaction that yielded a voluminous, porous ash-like product. The obtained ash was subsequently dried to remove residual moisture and then finely ground by pestle and mortar to obtain a uniform powder (Shanmugam and Rajan, 2026). Finally, the powder was calcined at 600 °C at muffle furnace to improve crystallinity and eliminate residual organic impurities, resulting at formation of pure $MnFe_2O_4$ nanoparticles.

2.2 Synthesis of Nanocellulose

Lignocellulosic fibers mainly consist of cellulose, hemicellulose, and lignin. Nanocellulose is produced from the α-cellulose fraction after suitable pretreatment to obtain purified cellulose. An alkali treatment (removes hemicellulose and other impurities), followed by a bleaching (eliminates lignin) result in purified cellulose suitable for nanocellulose extraction (Geremew *et al.* 2024).

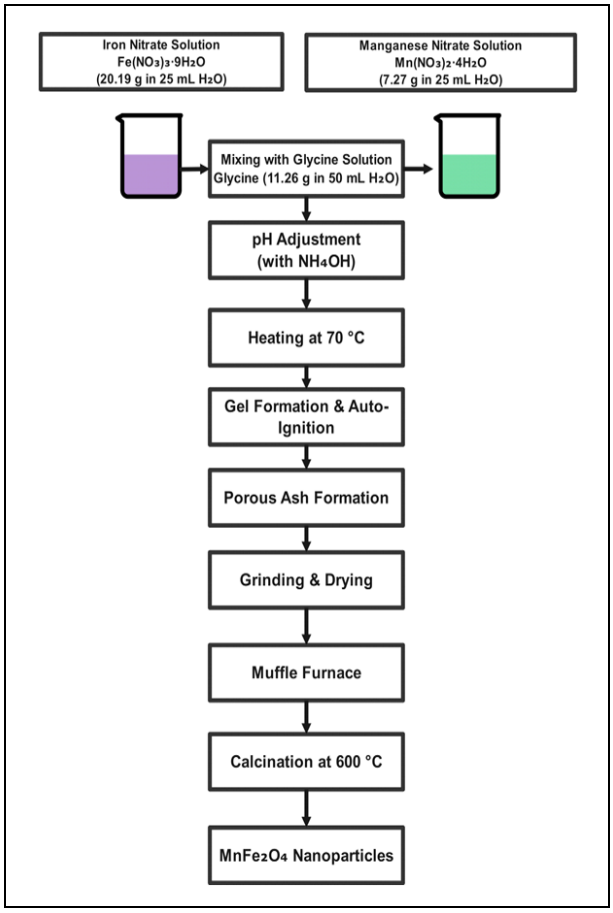


Fig. 1: Flow diagram of $MnFe_2O_4$ nanoparticle synthesis using sol–gel auto-combustion

2.3 Lignocellulose Pretreatment Process

Initially, the raw fibers were washed, dried, and milled into fine particles to remove surface impurities and reduce size. An alkaline pretreatment was then performed using immersing fibers in 5% NaOH solution under controlled temperature and duration. This treatment disrupts the fiber structure and eliminates wax, hemicellulose, and pectin components. The treated material was maintained in 5% NaOH for 3 hours with continuous stirring, while the temperature was kept at 80–100 °C, and subsequently washed until a neutral pH was obtained. This step was followed by a bleaching process to remove residual lignin and chromophoric compounds. The alkali-treated fibers was treated with 5% sodium chlorite ($NaClO_2$) solution under acidic conditions for 2–3 hours at 80–100 °C. The bleaching reaction degraded the remaining lignin and produced purified cellulose pulp, which was then thoroughly washed, filtered, and dried after reaching neutral pH.

2.4 Extraction Methods

Nanocellulose can be produced through two main approaches: chemical processing and mechanical treatment. Chemical routes include acid hydrolysis,

TEMPO-mediated oxidation, and ionic liquid processing, whereas mechanical techniques involve methods such as ultrasonication. In this study, the TEMPO-oxidation technique was adopted to obtain nanocellulose, as illustrated in Fig. 2.

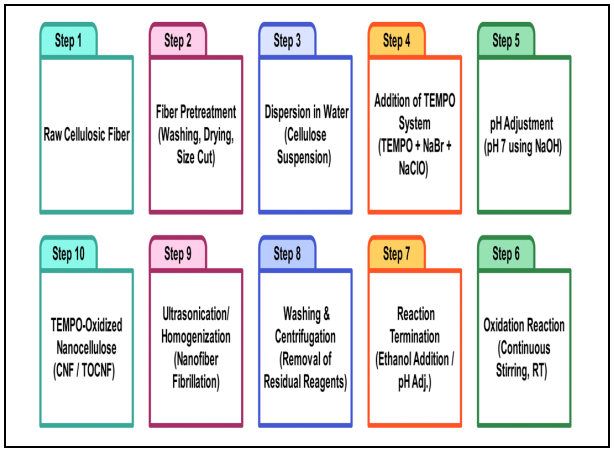


Fig. 2: TEMPO-oxidized nanocellulose preparation process

2.5 TEMPO Oxidation Method

TEMPO (2,2,6,6-tetramethylpiperidine-1-oxyl)-mediated oxidation was employed to obtain nanocellulose fibers (NCF). TEMPO, a water-soluble stable radical was used as the catalyst in the oxidation system. Initially, 1 g of purified cellulose was dispersed in 100 mL of DI water. A TEMPO solution prepared in 50 mL water was added to the cellulose suspension, followed by 0.1 g sodium bromide as a co-catalyst. The oxidation reaction was initiated by introducing 10% sodium hypochlorite (NaClO) while maintaining the pH around 7. The pH was regulated using sodium hydroxide, and the mixture was subsequently subjected to ultrasonication to ensure uniform dispersion and fibrillation. After completion of the reaction, the product was thoroughly washed and preserved at 4 °C. The resulting cellulose nanofibers possess abundant hydroxyl groups and a high specific surface area, and the yield was approximately 95%.

2.6 Synthesis of $MnFe_2O_4$-nanocellulose Composite

Nanocellulose–manganese ferrite composites were prepared in two mass ratios (50:50 and 75:25). The preparation procedure is illustrated in Fig. 3. For the 50:50 composition, 3 g of nanocellulose fibers was dispersed in 100 mL of DI water and stirred for 15 min using a magnetic stirrer to obtain a uniform suspension. Separately, 3 g of $MnFe_2O_4$ was dispersed in 100 mL of DI water and subjected to ultrasonication for 30 min to achieve good dispersion. The nanocellulose suspension was then added gradually to the ferrite dispersion, followed by ultrasonication for 1 h to ensure uniform mixing and interaction between the components. The resulting mixture was filtered to collect precipitate and washed with DI water to eliminate residual impurities. Finally, the collected product was dried at hot air oven at 70 °C for 3 hours to eliminate moisture, yielding $MnFe_2O_4$–nanocellulose composite.

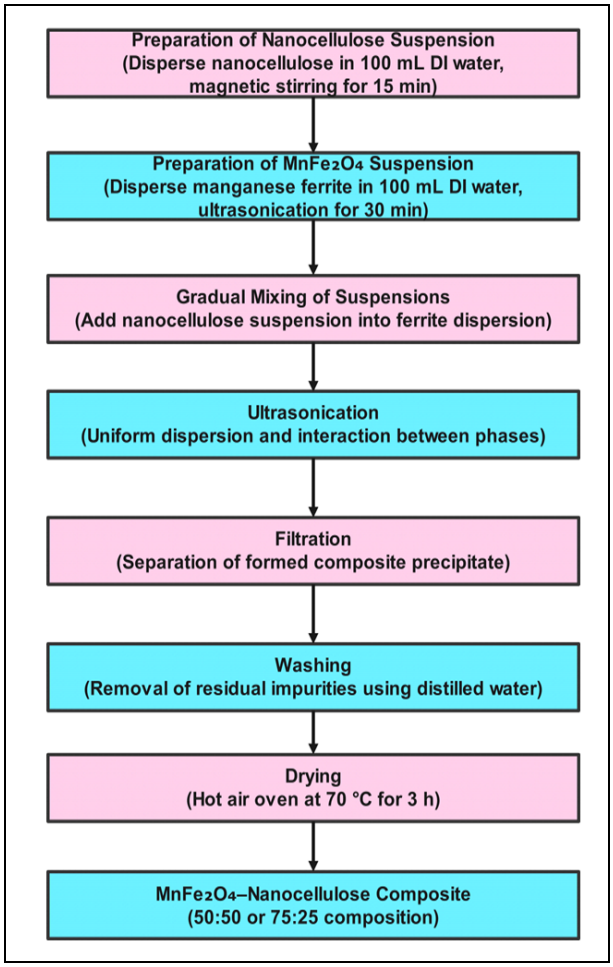


Fig. 3: Flow chart for the synthesis of manganese ferrite

For the 75:25 $MnFe_2O_4$–nanocellulose composite, 4.5 g of manganese ferrite was dispersed in 100 mL of DI water and ultrasonicated to obtain a uniform suspension. Separately, 1.5 g of nanocellulose was dispersed in 100 mL of DI water. The nanocellulose suspension was then introduced gradually into the ferrite dispersion, followed by ultrasonication for 3 hours to promote effective interaction between both phases. After sonication, the formed precipitate settled at the bottom. The mixture was filtered to separate the composite material, which was dried in a hot air oven 70 °C for 3 hours to eliminate remaining moisture and impurities, producing $MnFe_2O_4$–nanocellulose composite.

2.7 Characterization

The crystallographic characteristics of prepared samples were examined using X-ray diffraction (XRD, SmartLab SE) with diffraction data recorded in the 2θ

range 10–80°. Fourier transform infrared spectroscopy (FTIR) analysis was carried out by Alpha II (ATR mode) in the 400–4000 cm^{-1} spectral region with 4 cm^{-1} resolution and 16 scans to identify the functional groups. The surface morphology of nanocellulose fibers and $MnFe_2O_4$–nanocellulose composites was analyzed using scanning electron microscopy (SEM, ZEISS Gemini), providing a 3.0 nm resolution at 30 kV (SE mode). Energy-dispersive X-ray spectroscopy was additionally employed to determine the elemental composition of synthesized nanocomposites.

3. RESULTS AND DISCUSSION

3.1 X-Ray Diffraction

The XRD patterns of $MnFe_2O_4$, NCF, and the 50:50 and 75:25 composites are presented in Fig. 4. For manganese ferrite, diffraction profile shows six characteristic peaks located at 22.7°, 30.6°, 33.7°, 45.5°, 58.5°, and 63.7°. The strongest diffraction peak appears at 38.7°. The interplanar spacing (d-spacing) was determined using Bragg's law based on the measured 2θ values, while crystallite size was estimated from full width at half maximum of diffraction peaks using the Scherrer eqn (Eq. 1) (Nayebi and Fallah, 2026) :

$$D = \frac{0.9\lambda}{\beta \cos\theta} \quad \ldots (1)$$

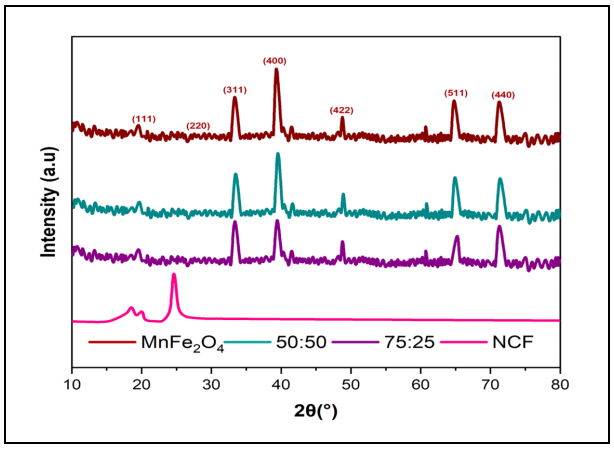


Fig. 4: XRD patterns of $MnFe_2O_4$, NCF, and the 50:50 and 75:25 composites

where D denotes crystallite size (Å), λ denotes wavelength of incident X-ray radiation, and β corresponds to full width at half maximum of diffraction peak.

The calculated crystallite size of $MnFe_2O_4$ nanoparticles was found to be in the range 15–20 nm. The interplanar spacing and Miller indices (hkl) for different Bragg diffraction angles of $MnFe_2O_4$ and nanocellulose fibers (NCF) are presented in Table 1 and Table 2, respectively.

Table 1. MF Bragg angle–spacing values

2θ (°)	Miller Indices (hkl)	d-Spacing (Å)
22.7	(111)	3.914
30.6	(220)	2.919
33.7	(311)	2.657
38.7	(400)	2.325
45.5	(422)	1.992
58.5	(511)	1.576
63.7	(440)	1.460

Table 2. NCF interplanar spacing values

2θ (°)	Miller Indices (hkl)	d-Spacing (Å)
18.2	(110)	4.870
22.5	(200)	3.948

For nanocellulose fibers, the characteristic diffraction peaks appear at 2θ ≈ 18.3° and 19.9°. Another peak at 24.6° shows the highest intensity. The broad diffraction feature indicates the semi-crystalline structure of cellulose, whereas the sharper peak confirms the presence of ordered crystalline regions. These reflections correspond to the (100) and (020) crystallographic planes of cellulose. The estimated crystallite dimension of the nanocellulose fibers lies in the range 20–30 nm.

For the $MnFe_2O_4$–nanocellulose composite with a 50:50 ratio, diffraction peaks appear at 2θ values of 22.20°, 25.94°, 33.50°, 38.69°, 45.97°, 54.99°, and 58.72°. The reflection at 63.89° corresponds to the characteristic peak of nanocellulose, confirming its presence within the composite structure. The remaining peaks at 25.94°, 33.41°, 38.40°, 45.59°, 54.99°, and 63.60° correspond to the spinel structure of $MnFe_2O_4$, indicating the successful incorporation of ferrite particles. A similar diffraction profile is observed for 75:25 $MnFe_2O_4$–NCF composite, where the 25.94° peak again confirms nanocellulose incorporation. In both composites, the intensity of the cellulose peak decreases compared with pure nanocellulose, suggesting interaction among ferrite nanoparticles and cellulose matrix. The calculated lattice spacing values for the composite peaks are consistent with those of the individual materials, as summarized in the tables. The introduction of nanocellulose leads to a slight reduction in overall crystallinity, particularly in the composite containing 25% nanocellulose. The particle size distribution histogram indicates that average particle size lies in range 60–120 nm for the 50:50 composite and 40–110 nm for the 75:25 composite, with the majority of particles concentrated around 80–100 nm and 70–90 nm, respectively. As observed in prior works, XRD analysis confirmed crystalline phase purity and spinel structure of synthesized $MnFe_2O_4$/(MWCNTs) nanocomposites. The diffraction patterns verified successful incorporation of $MnFe_2O_4$ nanoparticles with varying MWCNT contents

(0–20 wt.%) without forming secondary impurity phases (Mumtaz *et al.* 2021).

3.2 FTIR

The FTIR spectra of $MnFe_2O_4$, NCF, and the 50:50 and 75:25 composites are presented in Fig. 5. In the spectrum of pure $MnFe_2O_4$, a prominent peak appears near 580 cm^{-1}, corresponding to characteristic Fe–O stretching vibration at tetrahedral sites of the spinel ferrite structure. Additional broad peaks observed in the 3410 cm^{-1} and 1630 cm^{-1}were attributed to the O–H stretching and H–O–H bending vibrations of adsorbed moisture on the ferrite surface. The absence of distinct peaks corresponding to functional groups such as –OH, C=O, C–H, and C–C indicates that organic functional groups were not present in the pure $MnFe_2O_4$ sample.

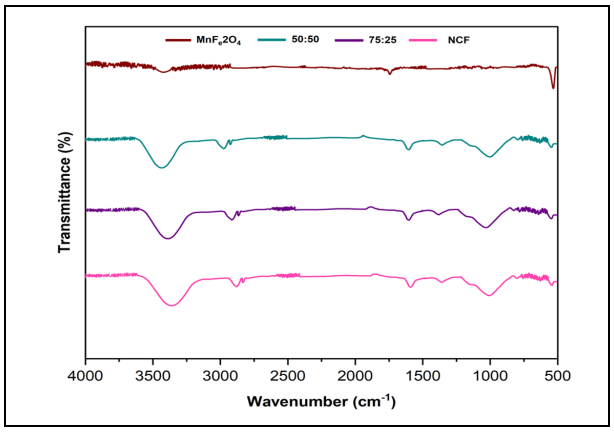


Fig. 5: FTIR spectra of the precursors and composites

Nanocellulose fibers are organic polysaccharide structures of repeating β-D-glucopyranose. The characteristic peaks appearing near 1370 cm^{-1} and 1055 cm^{-1} are associated with vibrational modes of the pyranose ring and C–O–C linkages. Additional peaks observed in the 3325 cm^{-1} and 2900 cm^{-1} region arise from stretching vibrations of functional groups like O–H and C–H present at cellulose backbone. he absorption band observed near 1630 cm^{-1} corresponds to O–H bending and partial C=O stretching vibrations. The FTIR features reflect both crystalline and amorphous domains of cellulose, indicating the semi-crystalline structure of nanocellulose fibers.

3.3 Fingerprint Region

The absorption peak at 1055 cm^{-1} indicates pyranose ring structure due to C–O–C stretching vibrations within glucopyranose units. The peak near 1370 cm^{-1} is associated with C–H bending vibrations of cellulose. The broad absorption bands observed near 3325 cm^{-1} and 2900 cm^{-1} correspond to O–H and C–H stretching vibrations, respectively, confirming the characteristic cellulose backbone structure.

3.4 Functional Group Region

A broad absorption peak between 3200–3400 cm^{-1} with a maximum near 3325 cm^{-1} corresponds to O–H stretching vibration associated with hydroxyl groups of the cellulose pyranose structure. A sharp peak observed at 2900 cm^{-1} was attributed to C–H stretching vibration of the cellulose backbone. Another peak appearing at 1630 cm^{-1} represents characteristic signal associated with O–H bending / C=O stretching vibration. The peak near 1370 cm^{-1} corresponds to C–H bending vibration. For the $MnFe_2O_4$–NCF composite (50:50), distinct peaks are detected at 580, 1055, 1625, 2918, and 3330 cm^{-1}.

A strong Fe–O stretching band around 580 cm^{-1} confirms the presence of manganese ferrite within the composite structure, which is absent in pure nanocellulose. Additionally, the peak at 3330 cm^{-1} shows O–H stretching vibrations of pyranose ring, related to intramolecular hydrogen bonding. The peak at 2918 cm^{-1} in the composite arises from C–H stretching vibrations of the pyranose ring, confirming the incorporation of nanocellulose in the $MnFe_2O_4$ composite matrix.

Nanocellulose fibers exhibit both crystalline and amorphous cellulose domains. In pure nanocellulose, a peak at 1370 cm^{-1} is associated with C–H bending vibration of cellulose. The peak at 1630 cm^{-1} in nanocellulose corresponds to O–H bending / C=O stretching vibration. A similar peak at 1625 cm^{-1} in $MnFe_2O_4$–NCF (50:50) composite confirms the presence of cellulose-related functional groups within the hybrid structure. Additionally, the peak detected at 1055 cm^{-1} in the composite corresponds to C–O–C stretching vibrations of cellulose pyranose ring, indicating the retention of the cellulose backbone within the ferrite matrix. Table 3 shows the prominent peaks and their assignments.

Table 3. Bond regions of MF–NCF composites

Pure $MnFe_2O_4$ (Wave Number cm^{-1})	Pure Nanocellulose Fiber (Wave Number cm^{-1})	Nanocellulose–$MnFe_2O_4$ Composite (50:50) (Wave Number cm^{-1})	$MnFe_2O_4$–Nanocellulose Composite (75:25) (Wave Number cm^{-1})	Bond/Functional Group
580	-	580	580	Fe–O stretching
-	1055	1055	1050	C–O–C stretching
-	-	–	–	C–C (pyranose ring)
-	-	–	–	C–C stretching
-	1370	–	–	C–H bending
1630	1630	1625	1625	O–H bending / C=O stretching
-	2900	2918	2915	C–H stretching
3410	3325	3330	3320	OH Stretching

For the $MnFe_2O_4$–nanocellulose composite with a 75:25 ratio, distinct FTIR absorption peaks appear at 580, 1050, 1625, 2915, and 3320 cm^{-1}. In the fingerprint region, the strong Fe–O stretching peak near 580 cm^{-1} corresponds to the characteristic vibration of the $MnFe_2O_4$ spinel structure, confirming the presence of ferrite within the composite. A broad peak at 3320 cm^{-1} was attributed to O–H stretching vibration of hydroxyl groups in the cellulose pyranose units, associated with intramolecular hydrogen bonding (O–H···O). The peak at 2915 cm^{-1} arises from C–H stretching vibrations of the pyranose ring, indicating the incorporation of nanocellulose within the composite matrix, since this band is absent in pure $MnFe_2O_4$. The peak at 1625 cm^{-1} corresponds to O–H bending / C=O stretching vibration, confirming the inclusion of cellulose-related functional groups in the hybrid material. These spectral features collectively verify the successful formation of the $MnFe_2O_4$–nanocellulose composite structure.

In pure nanocellulose fibers, a distinct peak appears at 1055 cm^{-1}, corresponding to C–O–C stretching vibration of glycosidic linkage, which confirms the presence of the pyranose ring structure in cellulose. Peaks observed at 1050 cm^{-1} and 1055 cm^{-1} in the $MnFe_2O_4$–NCF (75:25) composite further indicate the retention of the cellulose pyranose framework within the hybrid material. The FTIR analysis demonstrates that manganese ferrite contributes the characteristic Fe–O metal–oxygen bond, while nanocellulose provides organic functional groups like O–H, C–H, and C–O–C, confirming the coexistence of both inorganic ferrite and organic cellulose components in the composite structure. In a previous study, FTIR spectra exhibited peaks associated with C–O, C–H–C, and C=C groups, confirming partial surface functionalization of $MnFe_2O_4$ and $Mn_{0.95-x}Ga_{0.05}Sr_xFe_2O_4$ ferrite nanoparticles synthesized by the sol–gel route (Hernández-Castillo *et al.* 2025).

3.5 SEM Studies

The morphological characteristics of $MnFe_2O_4$ nanoparticles were examined using scanning electron microscopy to evaluate shape, distribution and particle size. Fig. 6 and Fig. 7 present SEM micrographs of $MnFe_2O_4$ and particle distribution, which were further analyzed using ImageJ software. In the micrograph recorded at a magnification of 30,000×, approximately 100 particles were identified for size analysis. The SEM images reveal relatively uniform, mono-dispersed particles with a predominantly cubic morphology, exhibiting a narrow particle size distribution. Previous analysis of $MnFe_2O_4$ spinel ferrite nanoparticles indicated that the FESEM images had irregularly shaped clusters with a wide particle size distribution, suggesting low aggregation (Ali *et al.* 2025). The $MnFe_2O_4$ sample calcined at 600 ℃ for 5 hours shows partial particle agglomeration, intrinsic magnetic interactions between ferrite particles and surface attractive forces such as van der Waals interactions. Furthermore, the SEM images obtained at 30,000× magnification indicate the presence of a porous surface morphology in the $MnFe_2O_4$ particles.

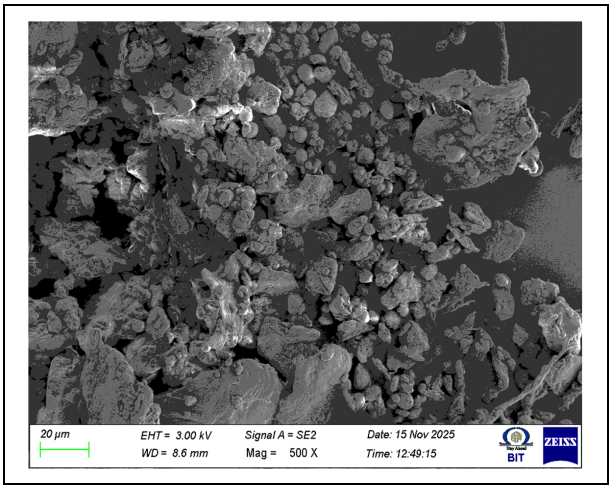


Fig. 6: SEM micrograph of $MnFe_2O_4$

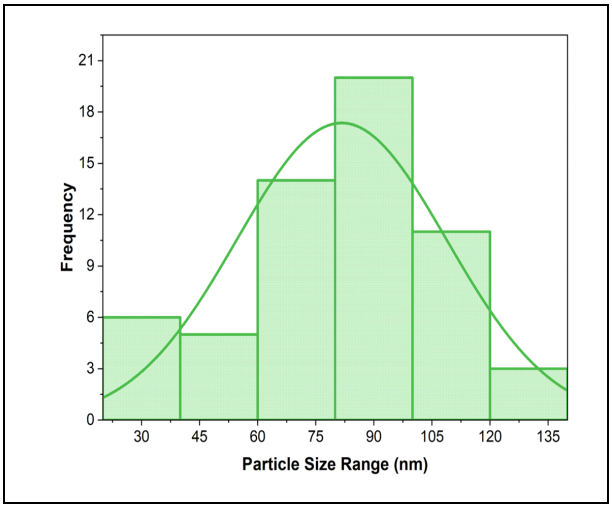


Fig. 7: Particle distribution of $MnFe_2O_4$

Multiple particles were scaled and recorded, and the obtained measurements were tabulated to construct a particle size distribution histogram. Histogram illustrates distribution of particles with different size ranges, enabling determination of the average size. The analysis indicates that the particle size varies between 60 and 120 nm, which is consistent with crystallite size estimated from XRD analysis.

The SEM micrographs of nanocellulose fibers confirm the formation of interconnected fibrillar networks, as shown in Fig. 8. The images reveal that the fiber surfaces are relatively rough and irregular, indicating effective fibrillation of cellulose into nanoscale structures. The histogram analysis (Fig. 9) indicates that the average diameter of nanocellulose fibers lies in the range 15–35 nm. These nanoscale

dimensions are consistent with crystallite size estimated from XRD results, confirming successful formation of nanocellulose fibers.

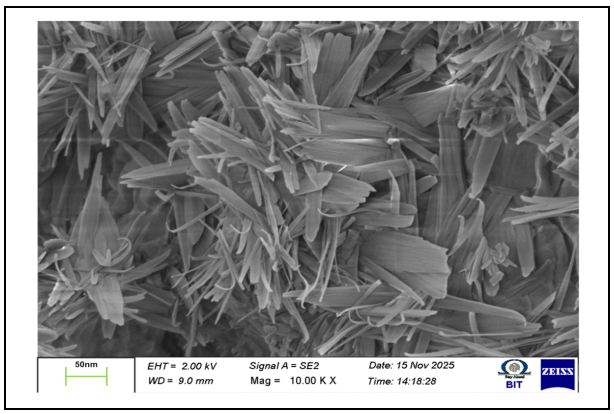


Fig. 8: SEM micrograph of nanocellulose fibers

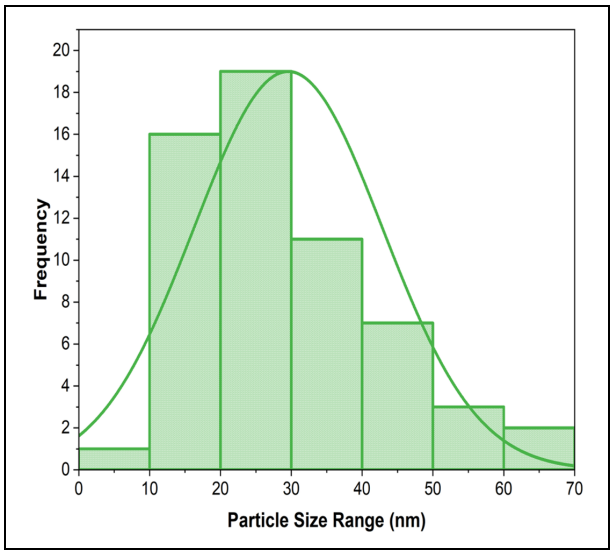


Fig. 9: Nanocellulose particle size distribution

The results confirm that nanocellulose fibers with a high specific surface area were successfully produced using the TEMPO-mediated oxidation technique. The large surface area enhances chemical reactivity and surface interaction capability of the fibers. Furthermore, the nanocellulose obtained from bamboo fibers exhibits surface characteristics that promote effective adhesion and interaction with metal oxide nanoparticles such as manganese ferrite, facilitating the formation of stable hybrid nanocomposite structures.

The SEM micrographs of the $MnFe_2O_4$–nanocellulose composite (50:50) show minor particle agglomeration, as illustrated in Fig. 10. The particle size distribution histogram generated from the SEM analysis (Fig. 11) indicates that the composite exhibits relatively smaller particle sizes. This reduction in particle size can be attributed to the higher proportion of nanocellulose fibers with nanoscale dimensions, which promotes better dispersion and restricts the growth of ferrite particles within the composite matrix.

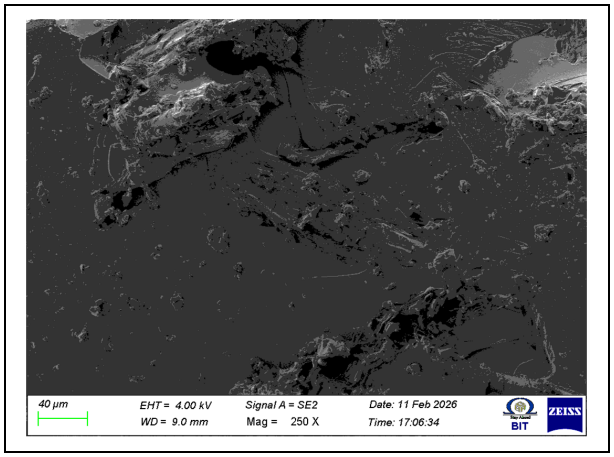


Fig. 10: SEM morphology of 50:50 composite

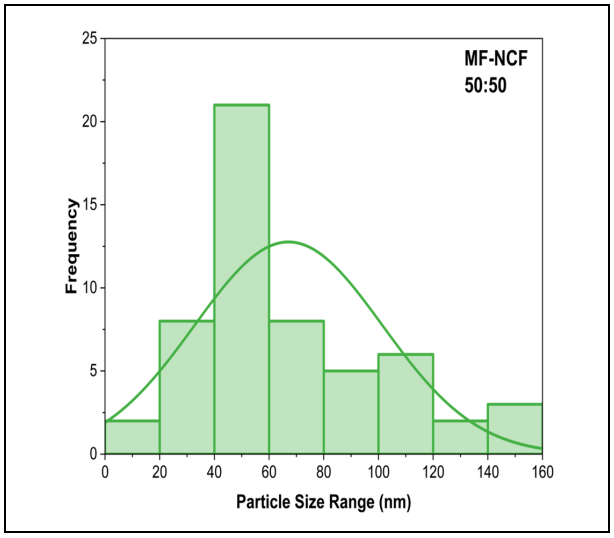


Fig. 11: Particle size distribution of MF–NCF

Fig. 12 presents the SEM micrograph of the $MnFe_2O_4$–nanocellulose composite (75:25). From the particle size distribution histogram (Fig. 13), the particle size for this composite is found to lie in the range 40–110 nm. Compared with the 50:50 composite, the average particle size is relatively larger, which can be attributed to the higher proportion of $MnFe_2O_4$ particles present in the composite. The SEM images also reveal partial particle agglomeration. Moreover, the composite exhibits a porous morphology with a high surface-to-volume ratio, a structural feature that is beneficial for gas sensing applications requiring rapid response and high sensitivity.

3.6 Elemental Analysis

EDAX spectrum of $MnFe_2O_4$ nanoparticles (Fig. 14) confirms the elemental composition corresponding to manganese ferrite. The detected

elements are consistent with the stoichiometric composition of $MnFe_2O_4$ based on its molecular formula. The quantitative elemental analysis obtained from EDAX provides both atomic and weight percentages of the constituent elements. The calculated atomic and molar compositions of manganese ferrite derived from the molecular formula are presented in Table 4.

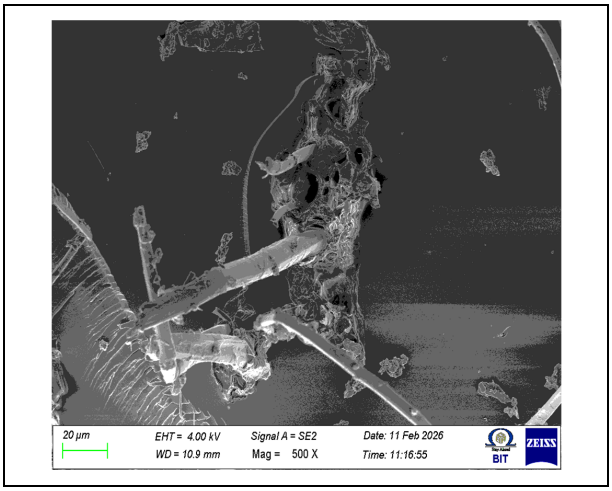


Fig. 12: SEM micrograph of 75:25 composite

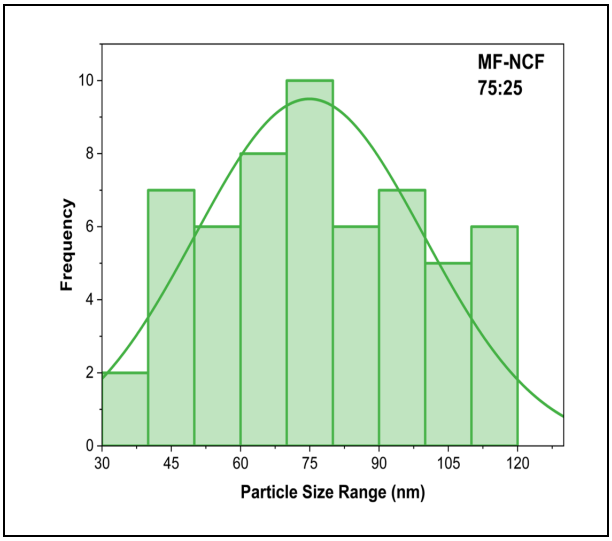


Fig. 13: Particle size distribution of MF–NCF

The EDAX analysis of nanocellulose fibers is presented in Fig. 15. The spectrum shows two dominant peaks corresponding to carbon (C) and oxygen (O), confirming the elemental composition of cellulose. A strong carbon peak is observed at approximately 3.7 keV, while the oxygen peak appears near 5.2 keV, indicating that these two elements constitute the primary chemical structure of nanocellulose. Nanocellulose is composed of repeating β-D-glucopyranose units. The elemental composition derived from the analysis indicates that carbon and oxygen are the major constituents, which agrees with the typical chemical structure of cellulose and confirms the successful formation of nanocellulose fibers.

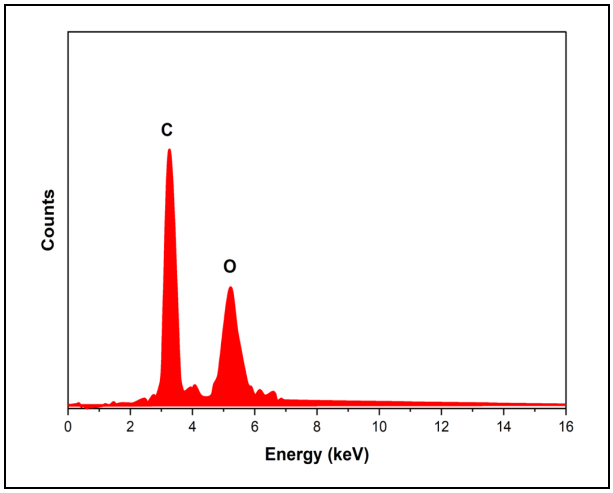


Fig. 14: EDX spectrum of $MnFe_2O_4$

Table 4. Molar and atomic composition

Element	Stoichiometric Atomic Ratio in $MnFe_2O_4$	Atomic Mass (g/mol)	Contribution to Molar Mass (g/mol)	Molar Fraction (%)	Atomic Fraction (%)
Manganese	1	54.938	54.938	23.82	14.29
Iron	2	55.845	111.69	48.43	28.57
Oxygen	4	15.999	63.996	27.75	57.14
Total	7	–	230.624	100	100

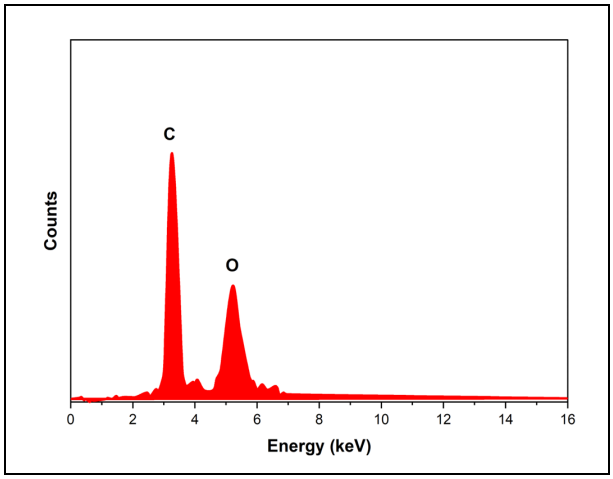


Fig. 15: EDAX of nanocellulose fibers

The first composite sample consists of $MnFe_2O_4$–nanocellulose fibers with a 50:50 weight ratio, prepared by mixing equal masses of manganese ferrite and nanocellulose during synthesis. A portion of the nanocellulose existed in a gel-like dispersion containing cellulose molecular chains. The EDAX spectrum of the composite confirms the presence of manganese (Mn), iron (Fe), oxygen (O), and carbon (C) elements. The signals of Mn and Fe correspond to the $MnFe_2O_4$ ferrite

phase, while C and O originate from the nanocellulose structure. The quantitative elemental analysis obtained from EDAX provides both weight percentage and atomic percentage of the detected elements. The calculated atomic and molar compositions of $MnFe_2O_4$ derived from the EDAX data are presented in Table 5, while the corresponding weight and atomic percentages obtained from the EDAX spectrum are summarized in Table 6.

Table 5. EDX composition of $MnFe_2O_4$

Element	Weight [%]	Atomic [%]	Error [%]
Carbon	64.2	70.8	6.0
Oxygen	35.8	29.2	5.3
Total	100.0	100.0	—

Table 6. Elemental weight and atomic composition

Element	Theoretical Weight (%)	EDS Weight (%)	Theoretical Atomic (%)	EDS Atomic (%)
Carbon	–	64.2	–	70.8
Oxygen	–	35.8	–	29.2

EDAX analysis of the $MnFe_2O_4$–nanocellulose composite is shown in Fig. 16. The spectrum exhibits characteristic peaks corresponding to oxygen (O), carbon (C), manganese (Mn), and iron (Fe), confirming the successful incorporation of ferrite nanoparticles within the nanocellulose matrix. The low-energy peaks around ~1.8 keV and ~2.6 keV correspond to oxygen and carbon, which mainly originate from the glucopyranose units of nanocellulose. In contrast, two strong peaks appearing at approximately ~10 keV and ~11.5 keV are attributed to Mn and Fe, indicating the presence of the $MnFe_2O_4$ ferrite phase. The carbon signal arises from the cellulose backbone, while oxygen is contributed by both the cellulose structure and the metal oxide lattice of $MnFe_2O_4$. The prominent Mn and Fe peaks further verify the successful deposition of ferrite nanoparticles on the nanocellulose fibers. Overall, the EDAX results confirm the coexistence of C, O, Mn, and Fe elements, validating the formation of the $MnFe_2O_4$–nanocellulose composite structure. In prior studies, elemental composition of the synthesized $Mn_{1-x}Zn_x\ Fe_2O_4$ nanoparticles was confirmed through EDAX analysis. The spectra verified the presence of Mn, Fe, Zn, and O elements, indicating the successful formation and compositional integrity of the ferrite nanoparticles (Kogulakrishnan *et al.* 2025). A slight reduction in oxygen content may be attributed to moisture evaporation during ferrite formation, while a minor aluminum impurity (~1.6 wt%) is also detected. These results confirm the successful formation of the $MnFe_2O_4$–nanocellulose composite with a 50:50 ratio, and the corresponding weight and atomic percentages are summarized in Table 7.

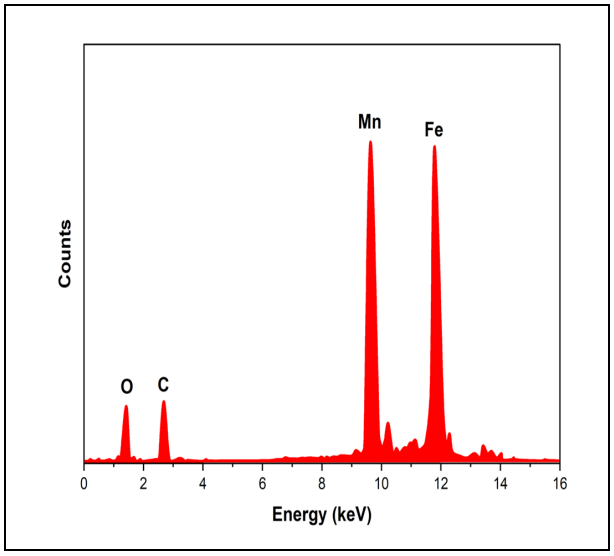


Fig. 16: EDX spectrum of MF–NCF composite

Table 7. Weight and atomic composition (50:50)

Element	Weight	Atomic	Error
C K	9.2	22.6	10.5
O K	13.8	33.4	8.2
Mn K	37.6	22.1	4.3
Fe K	39.4	21.9	3.9

The EDAX spectrum of the $MnFe_2O_4$–nanocellulose composite (75:25) is shown in Fig. 17. The spectrum displays distinct elemental peaks corresponding to manganese (Mn), iron (Fe), oxygen (O), and carbon (C), confirming the successful incorporation of ferrite nanoparticles into the nanocellulose matrix. The low-energy peaks observed around approximately 1.8–2.5 keV correspond to oxygen and carbon, which originate mainly from the glucopyranose units and hydroxyl groups of nanocellulose. In contrast, the strong peaks appearing at about 9.8–10 keV and 11–12 keV are attributed to manganese and iron, respectively, indicating the presence of the $MnFe_2O_4$ ferrite phase. The oxygen signal arises from both the ferrite oxide lattice and the cellulose structure, while carbon is contributed entirely by the nanocellulose fibers. The prominent Mn and Fe peaks confirm the formation and successful incorporation of $MnFe_2O_4$ nanoparticles within the nanocellulose matrix, supporting the synthesis of the $MnFe_2O_4$–nanocellulose composite with a 75:25 composition. Similarly, the previous studies demonstrated that, the EDAX characterization confirmed the elemental distribution in the Al_2O_3@$MnFe_2O_4$ nanocomposite. The analysis validated the presence of Al, Mn, Fe, and O elements, demonstrating the successful incorporation of Al_2O_3 into the $MnFe_2O_4$ nanostructure (Kondalkar *et al.* 2022).

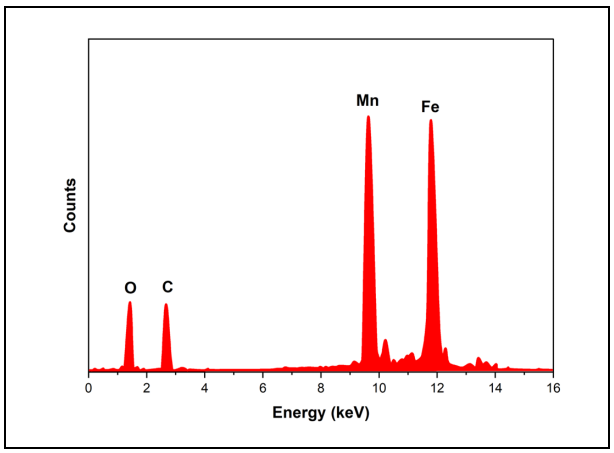


Fig. 17: EDX spectrum of MF–NCF composite (75:25)

Table 8. EDX weight–atomic percentages of composite (75:25)

Element	Weight [%]	Atomic [%]	Error [%]
C K	4.8	12.5	10.8
O K	14.2	34.6	8.5
Mn K	40.5	26.0	4.2
Fe K	40.5	26.9	3.8

The measured elemental values are consistent with the expected composite composition. A slight reduction in oxygen content may be attributed to the evaporation of water molecules during the ferrite formation process. No additional impurity elements were detected in the EDAX analysis, confirming the purity of the synthesized composite material.

4. CONCLUSIONS

$MnFe_2O_4$–nanocellulose hybrid nanocomposites were successfully synthesized using a sol–gel auto-combustion method combined with TEMPO-mediated oxidation of bamboo-derived cellulose. The XRD analysis confirmed the formation of spinel $MnFe_2O_4$ nanoparticles with crystallite sizes in the range 15–20 nm, while nanocellulose fibers exhibited crystallite sizes between 20–30 nm with characteristic diffraction peaks near 18.2° and 22.5°. The SEM observations revealed that MnFe2O4 nanoparticles possessed particle sizes of approximately 60–120 nm, whereas nanocellulose fibers showed nanoscale diameters of about 15–35 nm. The MnFe2O4–nanocellulose composites prepared in 50:50 and 75:25 weight ratios exhibited particle size distributions of 60–120 nm and 40–110 nm, respectively, demonstrating improved dispersion of ferrite nanoparticles within the nanocellulose matrix. The FTIR spectra showed characteristic Fe–O stretching peaks near 580 cm^{-1} along with cellulose functional groups at 1050–1055 cm^{-1} (C–O–C stretching), 2915–2918 cm^{-1} (C–H stretching), and 3320–3330 cm^{-1} (O–H stretching), confirming the successful formation of the hybrid composites. The EDAX analysis further verified the elemental composition with Mn and Fe contents of approximately 37.6–40.5 wt% and 39.4–40.5 wt%, respectively, along with oxygen (13.8–14.2 wt%) and carbon (4.8–9.2 wt%), indicating the purity and correct stoichiometry of the composite. The synthesized $MnFe_2O_4$–nanocellulose nanocomposites exhibited porous morphology, high surface area, and reduced nanoparticle agglomeration, which enhance structural stability and functional performance. These characteristics make the developed hybrid nanocomposites promising candidates for advanced applications such as gas sensing, environmental monitoring, catalytic systems, and other functional nanomaterial-based technologies.

FUNDING

This research received no specific grant from any funding agency in the public, commercial, or not-for-profit sectors.

CONFLICTS OF INTEREST

The authors declare that there is no conflict of interest.

COPYRIGHT

This article is an open-access article distributed under the terms and conditions of the Creative Commons Attribution (CC BY) license (http://creativecommons.org/licenses/by/4.0/).

REFERENCES

Ali, I. O., Salama, T. M., Nady, H., Seaf, E. T. A. and Mohamed, H. H., Fabrication and engineering of cd-doped $MnFe_2O_4$ spinel ferrites for hydrogen evolution in alkaline media, *Inorg. Chem. Commun.*, 182, 115353(2025). https://doi.org/10.1016/j.inoche.2025.115353

Amjad, M., Bibi, I., Iqbal, M., Kamal, S., Mustafa, G., Nouren, S., Taj, B., Nazar, N., Alwadai, N. and Nazir, A., Interfacial coupling-driven enhancement of capacitance in $MnFe_2O_4$/NiO nanocomposites synthesized via sol–gel auto-combustion, *J. Sol-Gel Sci. Technol.*, 117(3), 60(2026). https://doi.org/10.1007/s10971-025-07094-9

Asmare, F. W., Liu, X., Qiao, G., Li, R., Babu K, M. and Wu, D., Investigation and application of different extraction techniques for the production of finer bamboo fibres, *Adv. Bamboo Sci.*, 7, 100070(2024). https://doi.org/10.1016/j.bamboo.2024.100070

Chakkour, M., Moussa, M. O., Khay, I., Balli, M. and Ben Zineb, T., Hygroscopic aging cycles of bamboo fiber/epoxy composites: Comparative study between distilled water and sea water, *Indus. Crops Prod*., 209, 117957(2024). https://doi.org/10.1016/j.indcrop.2023.117957

Dhasharatha, U., Vinod, G., Rajashekhar, K., Mallesh, D., Sreematha, B. and Laxman, N. J., Photocatalytic degradation of rhodamine B using Yb3+-Doped Zn-Mg ferrites synthesized via conventional sol-gel auto-combustion method, *Ceram. Int*., 50(22), 46940–46961(2024). https://doi.org/10.1016/j.ceramint.2024.09.046

Fourari, A., Chakkour, M., Ould, M. M., Khay, I. and Ben, Z. T., Thermal aging effects on microstructural, sorption and mechanical properties of bamboo fibers, Cellulose, 33(2), 695–716(2026). https://doi.org/10.1007/s10570-025-06909-w

Geremew, A., De Winne, P., Demissie, T. A. and De Backer, H., Surface modification of bamboo fibers through alkaline treatment: Morphological and physical characterization for composite reinforcement, *J. Eng. Fib. Fab*., 19, 248764(2024). https://doi.org/10.1177/15589250241248764

Ghaly, M., Youssef, M. A. and Borai, E. H., Efficient separation of cerium from rare earth elements and major impurities using low-cost manganese ferrites from highly acidic solutions, *J. Environ. Chem. Eng*., 12(6), 114588(2024). https://doi.org/10.1016/j.jece.2024.114588

Hammou, Z., Makhloufi, S., Aissaoui, R., Hachani, S. E., Achour, A., Fodil, H., Ben, A. M. L. and Boudiaf, M., Sol–gel synthesis and detailed characterization of manganese ferrite nanoparticle for the enhanced photocatalytic degradation of methylene blue, crystal violet, and neutral red dyes, *React. Kine. Mech. Catal.,* 138(6), 4319–4337(2025). https://doi.org/10.1007/s11144-025-02923-y

Hernández-Castillo, F. J., Cortés-Hernández, D. A. and Escobedo-Bocardo, J. C., Effect of the synthesis method on the heating ability and physicochemical properties of gallium and strontium-substituted manganese ferrites*, Mater. Chem. Phy*., 337, 130623(2025). https://doi.org/10.1016/j.matchemphys.2025.130623

Kogulakrishnan, K., Nithiyanantham, S., Mohan, R., Giridharan, N. V, Silambarasan, S., Venkadesh, A., Latha, V., Gunasekaran, B. and Palaniappan, L., Structural, electrical and magnetic studies on Zn doped $MnFe_2O_4$ nanoparticles with via Sol-Gel approach, *J. Mol. Struct*., 1321, 140026(2025). https://doi.org/10.1016/j.molstruc.2024.140026

Kondalkar, M., Fegade, U., Kanchi, S., Altalhi, T., Suryawanshi, K. E. and Patil, A. M., Adsorption of Cr(VI) on Ultrafine Al_2O_3-doped $MnFe_2O_4$ nanocomposite surface: Experimental and theoretical study using double-layer modeling, *J. Phy. Chem. Sol*., 163(2022). https://doi.org/10.1016/j.jpcs.2021.110544

Mahmoud, Z. H., Hussein, S. A., Hassan, E. A., Abduvalieva, D., Mhaibes, R. M., Kadhum, A. A. H., Nasier, S. J., Kianfar, E. and Faghih, S., Characterization and catalytic performance of rGO-enhanced $MnFe_2O_4$ nanocomposites in CO oxidation, *Inorg. Chem. Commun.,* 169, 113037(2024). https://doi.org/10.1016/j.inoche.2024.113037

Mumtaz, M., Mubasher, and Ali, M., Structural, Dielectric and Electric Modulus Studies of $MnFe_2O_4$/(MWCNTs) x Nanocomposites, *J. Mater. Eng. Perform*., 30(6), 4494–4503(2021). https://doi.org/10.1007/s11665-021-05721-4

Nayebi, R. and Fallah, S. A., Simple and eco-friendly synthesis of octahedral $MnFe_2O_4$ using green tea and application in congo red dye adsorption, *Int. J. Environ. Sci. Technol.,* 23(1), 54(2026). https://doi.org/10.1007/s13762-025-06883-7

Oviya, K. J. and Sivagurunathan, P., Structural, Magnetic and Electrochemical Properties of Nickel Manganese Ferrite (Ni_xMn_1-xFe_2O_4) Nanoparticles Prepared via Coprecipitation Method, *Asian J. Chem.,* 36(10), 2375–2384(2024). https://doi.org/10.14233/ajchem.2024.32404

Pandey, B., Srivastava, R. C., Joshi, C. S. and Verma, H. K., Effect of cerium ion doping: Alteration in structural, dielectric and magnetic properties of manganese ferrite nanoparticles, *Physica B: Condensed Matter,* 711, 417302(2025). https://doi.org/10.1016/j.physb.2025.417302

Riaz, T., Tahira, F., Mansoor, S., Shahid, S., Javed, M., Shahzadi, T., Zidan, A., Seçkin, C. İ., Zaib, M., Bahadur, A., Iqbal, S., Mahmood, S., Alzahrani, E. and Farouk, A. E., Highly operative removal of amoxicillin (AMX) from aqueous solution by $MnFe_2O_4$ nanoparticles and carboxy methyl cellulose (CMC) composite, *Polyhedron*, 263, 117195(2024). https://doi.org/10.1016/j.poly.2024.117195

Sarfraz, Z., Hussain, M., Mumtaz, M., Luqman, M., Kaleem, M. and Raza, M., Impact of Cobalt Doping on the Structural and Frequency-Dependent Dielectric Properties of Manganese Ferrites for Advanced Energy Storage Applications, *J. Electron. Mater*., 55(1), 565–581(2026). https://doi.org/10.1007/s11664-025-12534-x

Shanmugam, Y. and Rajan, B. D., Synthesis, characterisation and antibacterial activity of green synthesised manganese ferrite, *Chem. Phy. Impact*, 12, 101011(2026). https://doi.org/10.1016/j.chphi.2026.101011

Teymur, Y. A. and Güzel, F., Microwave-assisted synthesis, characterization, and oxytetracycline antibiotic sorption performance of a novel magnetic nanohybrid material: $MnFe_2O_4$@black cumin solid waste-derived activated carbon, *J. Environ. Chem. Eng.,* 12(3), 112641(2024). https://doi.org/10.1016/j.jece.2024.112641

Ullah, N., Sadiq, S., Khan, S., Ismail, M. and Sadiq, M., PEG-Modified $MnFe_2O_4$ Nanoparticles: Polymer-Assisted Enhancement in Photocatalytic Degradation and Mechanistic Insights, *J. Appl. Polym. Sci*., 143(10), e70208(2026). https://doi.org/10.1002/app.70208

Verma, Y. K., Singh, A. K., Paswan, M. K. and Gurmaita, P. K., A novel approach to extract and characterize vacuum-pressurized bamboo fibers using mechano-chemical techniques, *J. Wood Chem. Technol*., 43(4), 230–242(2023). https://doi.org/10.1080/02773813.2023.2224301

Verma, Y. K., Singh, A. K., Paswan, M. K. and Prashanth, S., Mechano-chemical extraction and characterization of tannic acid-functionalized bamboo fibers from vacuum-pressure impregnation (VPI) treated and untreated sources to enhance mechanical properties of fiber-reinforced polymer (FRP) laminated composites, *Wood Mater. Sci. Eng*., 21(1), 498–513(2026). https://doi.org/10.1080/17480272.2024.2436517

Vermani, S., Kaur, P. and Kaur, V., Characterization of Thermally Stable Bamboo Fiber Sheet Loaded with Cobalt Ferrite Nanoparticles, *J. Electron. Mater*., 53(4), 1796–1806(2024). https://doi.org/10.1007/s11664-024-10917-0

Yasar, M. and Javed, K., Synthetic Studies of Aluminum-Doped $Zn_{0.5}Mn_{0.5}Al_xFe_{2-x}O_4$ Ferrite for Photocatalytic Degradation of Atrazine Under Visible Light, *Arab. J. Sci. Eng.,* 50(9), 6471–6484(2025). https://doi.org/10.1007/s13369-024-09442-3